# Laser-induced fluorescence spectroscopy applied to electric thrusters

Stéphane Mazouffre

# Laser-induced fluorescence spectroscopy applied to electric thrusters

**Stéphane Mazouffre**
Electric Propulsion team
CNRS, ICARE
1c Avenue de la Recherche Scientifique
Orléans, 45071
France

stephane.mazouffre@cnrs-orleans.fr

## *ABSTRACT*

*This article presents an overview of the Laser-Induced Fluorescence (LIF) spectroscopy technique for diagnosing the plasma discharge and the beam of electric propulsion devices employed onboard satellites and robotic space probes for various types of maneuvers. Performing LIF experiments on atoms or ions appears to be a powerful way to get accurate insights into the physics at work in such thrusters. In this review emphasis is placed on the LIF underlying principles, time-averaged as well as time-resolved measurements, associated optical setup and experimental outcomes. A discussion about electric field determination by the LIF method is also given as this quantity is of prime relevance for many electric thrusters.*

## Contents

## 1.0 INTRODUCTION

In comparison with chemical engines, electric propulsion (EP) systems offer significant advantages for commercial and scientific space missions in terms of payload mass, launch cost and mission duration due to a fast propellant ejection speed that warrants a large propellant mass savings according to the Tsiolkovsky rocket equation [1]. Currently, electric propulsion systems are mostly employed for station keeping, attitude control, orbit raising and orbit transfer maneuvers of geosynchronous telecommunication satellites. The increase of electrical power available onboard the spacecraft on the one hand as well as the emergence of new technologies, especially in the field of micropropulsion, on the other hand could lead to new applications of electric propulsion in the near future, like moving of small, micro- and nano-satellites, end-of-life deorbiting, space tugs and space cargos. In addition, the development of high-power devices could generalize robotic space probe journeys towards far-off planets and asteroids. Electric propulsion technologies may be split into three broad categories according to the way thrust is generated: electrothermal, electrostatic and electromagnetic propulsion. These groups encompass numerous approaches and devices that cover a vast range of characteristics and performances [1–8].

Despite several decades of research devoted to electric thruster physics and the development of various technologies that cover a broad range of performances in terms of thrust, specific impulse and efficiency, many physical mechanisms that govern the behavior and the properties of the plasma discharge and the ion beam remain ill-understood and not well quantified. This lack of knowledge is clearly a limiting factor for various aspects of the EP technology: optimization of existing devices, expansion of the performance envelope, development and construction of novel and more efficient thruster architectures, utilization of alternative propellants, development of predictive numerical models, to only name a few. The field of EP is therefore an active field of R&D where the use and the development of sophisticated diagnostic tools is crucial to get precise data connected with the fundamental physical mechanisms at work. Among all possible methods to diagnose the plasma discharge and jet of EP systems, laser-aided approaches like absorption, fluorescence and scaterring techniques offer many advantages: a non intrusive, or weakly intrusive, character, a high spatial and temporal resolution, a high sensitivity, a high accuracy and the access to all quantities of relevance like particle density, temperature, velocity as well as electric and magnetic fields. On the other hand, there are of course drawbacks: the optical bench, which comprises the laser source, all optical components and the detection assembly, is usually

expensive, laser diagnostic techniques are cumbersome and data acquisition and treatment often require some experience and expertise.

Description of all available laser-aided diagnostic techniques for EP devices is out of the scope of this review. The present article solely focuses on the utilization of Laser-Induced Fluorescence (LIF) spectroscopy for electric thruster diagnosis and it shows how LIF can provide insights into the physics at work in the discharge and the beam of propulsion devices. The contribution is divided into several parts. The basic principles of the LIF spectroscopy technique are summarized in section 2.0. Single-photon and multi-photon excitation schemes are incorporated into this overview. After explaining the origin of the fluorescence light, we give the advantages and limitations of the technique and we present the various line broadening mechanisms. Examples of measured fluorescence lineshapes are given at the end. In section 3.0, we discuss the optical train, the fluorescence detection branch and the data acquisition system. In addition, 2D and 3D LIF setup are outlined. Section 4.0 deals with measurement of the velocity distribution function and associated macroscopic quantities like velocity, temperature and density. Two different ways for accessing the electric field are discussed in section 5.0. Indirect determination from the velocity profile, with or without using the moments of the Boltzmann's equation, is compared to direct determination that rests upon the Stark shift of highly-excited atomic levels. Explication of time-resolved LIF measurements are given in section 6.0 with emphasis on approaches using continuous lasers. Outcomes are illustrated with measurements of the time-varying ion velocity in Hall thrusters by way of a photon-counting technique. Finally, conclusions are drawn in section 7.0 and comments on time-resolved measurements and complementary techniques are given to close this contribution.

## 2.0 PRINCIPLE OF LIF SPECTROSCOPY

### 2.1 Fluorescence signal

The Laser-Induced Fluorescence spectroscopy technique offers the possibility of spatially and temporally resolved measurements of various quantities in complex media encountered in plasma physics and electric space propulsion [9–17]. LIF allows to measure molecule, atom and ion concentration in a specific quantum state, either in a relative way or in an absolute way when an appropriate calibration method of the fluorescence signal is applied. LIF also allows to acquire the particle Velocity Distribution Function (VDF), a fundamental statistical quantity that gives information about the thermodynamic state of the medium. From the VDF, or more generally from the fluorescence profile, one can extract the temperature, the mean velocity and the most probable velocity. Finally, the LIF technique enables to directly determine electric fields and magnetic fields in plasmas through the Stark effect and the Zeeman effect, respectively. In other fields like atomic physics and chemistry, the LIF diagnostic tool is employed to measure collision rates and radiative lifetime and to determine atomic and molecular energy level diagrams.

The principle of LIF spectroscopy is illustrated in Figure 1 with a two-level quantum system. Atomic population is transferred by optical pumping from the low energy quantum level $|i>$ to the high energy level $|j>$. An optical transition from one quantum state to another must obey selection rules based on various quantum numbers [18, 19]. The selection rules depend on the coupling scheme and on multipole order and type: dipole, quadrupole and octupole, and electric versus magnetic. However, a transition is never strictly forbidden. When the electric dipole rules are not applicable, the so-called forbidden case, transitions merely occur at a very low rate. The first step in Figure 1 is termed the absorption process [9–11]. It occurs when the energy of the incident photons matches the energy difference between the two levels. Subsequently, the level $|j>$ deexcites to a lower energy level $|k>$ by emitting light, the so-called fluorescence photons. The fluorescence light intensity provides information about the population of the initial state $|i>$. The population in

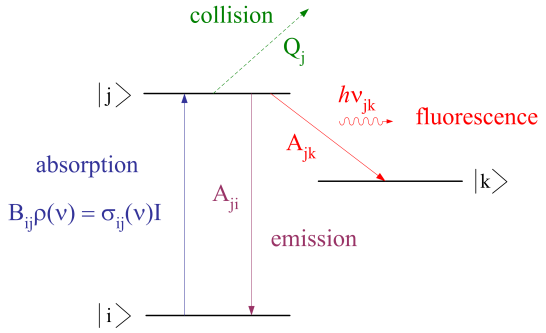


**Figure 1: Schematic of the LIF spectroscopy principle. Photons with energy $h\nu = E_j - E_i$ excite the $|i> \rightarrow |j>$ transition. Here fluorescence light corresponds to the spontaneous emission during decay to the $|k>$ level. $\rho$ is the spectral energy density, $B_{ij}$ is the Einstein coefficient for absorption, $I$ is the laser beam intensity and $\sigma$ is the absorption cross-section. $A$ are Einstein coefficients for spontaneous emission. $Q$ refers to quenching, i.e. non radiative deexcitation due to collisions.**

the $|j>$ level can also decay without generating light due to collision events with other particles like atoms and electrons. This non radiative deexcitation process is known as quenching and it must be accounted for when analyzing fluorescence spectra, especially when the density is the quantity of interest. When the wavelength of the laser beam incident photons is the same as the wavelength of the fluorescence photons, the LIF technique is said to be resonant. It is a special case of LIF spectroscopy which necessitates great attention as laser photons and fluorescence photons are indistinguishable in terms of energy.

A rigorous treatment of the laser-induced fluorescence process requires to apply quantum mechanics and to use the formalism of the semi-classical Maxwell–Bloch equations, which describe the dynamics of a two-state quantum system interacting with an electromagnetic wave [20]. However, in the weak laser beam energy limit, a classical approach based on rate equations can be used and it leads to results in agreement with the more sophisticated quantum approach [9–11].

The absorption process is here assumed to be linear, i.e. $N_\mathrm{i} >> N_\mathrm{j}$ where $N$ refers to the density. The population transfer $|i> \rightarrow |j>$ induced by photons of frequency $\nu$ reads:

$$\frac{d}{dt}N_\mathrm{i}(t) = -\sigma_\mathrm{ij}(\nu)\frac{I_L(t)}{h\nu}N_\mathrm{i}(t), \tag{1}$$

where $\sigma_\mathrm{ij}$ is the absorption cross-section in $\mathrm{m}^{-2}$, $I_L$ the laser beam intensity in $\mathrm{W\,m}^{-2}$ and $h$ is the Planck constant. In like manner the density change of the excited state $|j>$ is given by:

$$\frac{d}{dt}N_\mathrm{j}(t) = \sigma_\mathrm{ij}(\nu)\frac{I_L(t)}{h\nu}N_\mathrm{i}(t) - (A_\mathrm{j} + Q_\mathrm{j})N_\mathrm{j}(t), \tag{2}$$

where $A_\mathrm{j}$ is the probability of radiative deexcitation of level $|j>$ in $\mathrm{s}^{-1}$ and $Q_\mathrm{j}$ is the quenching rate in $\mathrm{s}^{-1}$. The quantity $A_\mathrm{j}$ is the sum of all Einstein coefficients for spontaneous emission of level $|j>$ and it corresponds to the reciprocal of the radiative lifetime $\tau_\mathrm{j}^\mathrm{rad}$:

$$A_\mathrm{j} = \sum_k A_\mathrm{jk} = \frac{1}{\tau_\mathrm{j}^\mathrm{rad}} \tag{3}$$

The number of fluorescence photons emitted at frequency $\nu$ per unit volume is:

$$n_\mathrm{jk}(\nu) = A_\mathrm{jk}\int_0^\infty N_\mathrm{j}(t)dt. \tag{4}$$

The total number of fluorescence photons recorded when scanning the absorption profile of the $|i> \rightarrow |j>$ optical transition is proportionnal to the density of atoms in state $|i>$:

$$n_{\text{fluo}} = K N_{\text{i}}(0) \frac{A_{\text{jk}}}{A_{\text{j}} + Q_{\text{j}}} \sigma_{\text{ij}} \int_{\nu} \int_{t} \frac{P_{\text{abs}}(\nu) \otimes P_L(\nu)}{h\nu} I_L(t)\, d\nu\, dt. \tag{5}$$

where $K$ is a constant linked to the optical detection system, $P_{\text{abs}}$ the absorption line profile, $P_L$ the laser beam spectral line shape and the operator $\otimes$ defines the convolution operation. In linear regime, that is when the saturation parameter $S$ is below 1, see section 2.4, the fluorescence signal varies linearly with the laser intensity. Equation 5 indicates the fluorescence signal depends upon:

- The lifetime of the upper state, which accounts for radiative processes and quenching: $\tau_{\text{j}} = (A_{\text{j}} + Q_{\text{j}})^{-1}$,
- The absorption cross-section and the Einstein $A$ coefficient of the fluorescence transition,
- The initial density of the probed state before firing the laser $N_{\text{i}}(0)$,
- The absorption line profile and the laser line profile,
- The laser beam intensity, i.e. the number of photons.

## 2.2 Advantages and limitations

Contrary to other techniques like electrostatic probes, Mach probes and mass spectrometry, the LIF spectroscopy technique is weakly intrusive. Addition of energy into the plasma medium with a laser beam leads to a change in the local thermodynamical equilibrium. Nevertheless, as long as the laser power density is low the induced perturbation of the measurable quantities is insignificant. At high laser energy, the equilibrium between atomic states is modified. In the worst case, atoms are ionized and molecules are dissociated, which strongly changes the local electron energy distribution function. For LIF experiments, the laser beam energy must therefore be kept as low as possible. In addition to being non-intrusive, LIF spectroscopy presents other advantages:

- One can select a species and an energy level,
- The spectral resolution is very high,
- The spatial and temporal resolutions are high,
- It is a high sensitivity technique with a detection limit around $10^{14}\,\text{m}^{-3}$.

The LIF technique also has drawbacks:

- The LIF processe is incoherent, that means the signal-to-noise ratio is relatively low,
- As shown in Equation 5, in order to obtain an absolute number density, the fluorescence yield must be calibrated. There are several methods:
  * The factor $K$, see Equation 5, can be asssed accounting for all contributions. This approach is however relatively inaccurate.
  * Measurements by absorption spectroscopy on the same transition [11]. This calibration method is relevant when the density is homogeneous throughout the medium as absorption is a line-of-sight measurement technique.

    * $K$ can be determined by means of Rayleigh scattering at the fluorescence wavelength [15, 21].
    * The integral of the fluorescence lineshape can be connected with the density using chemical titration [15]. This scheme only applies to ground-state atoms and molecules. In some cases, an alternative is to employ a noble gas [15].

- There is no laser sources available in the UV, VUV and XUV spectral ranges. This makes difficult access to ground-state atoms and molecules, which is the most populated state is low temperature plasmas. Laser beam with $\lambda < 250$ nm can however be produced using non-linear optical techniques [12, 22],
- Several parasitic effects can arise: Absorption of the laser beam in the plasma, absorption of fluorescence photons (optically thick medium), quenching, ionization of the gas (large beam energy, high energy photons), scattering of the laser beam by various components, saturation of the transition,

A tunable laser is needed to scan the absorption profile. There are different types of lasers whose wavelength can be adjusted over a broad range: solid-state lasers, dye lasers, laser diodes, quantum cascade lasers and optical parametric oscillators [23, 24]. All of them are suited for LIF experiments. One must also distinguish between continuous and pulsed mode of operation of a laser [23, 24]. A continuous wave (cw) laser, e.g. laser diodes, exhibits a very narrow bandwidth, typically in the femtometer range or below. Such lasers allows to directly observe the particle VDF in LIF measurements. Pulsed lasers are broad band and usually deliver a large amount of energy per pulse. The pulse duration can be as short as a few femtoseconds.

## 2.3 Line profile

### 2.3.1 Natural linewidth

The spontaneous or natural emission profile is a Lorentzian function of which the full width at half maximum $\Delta\nu_n$, the natural linewidth, is linked to the radiative lifetime, in compliance with the Heisenberg uncertainty principle:

- If $|i>$ is a ground-state ($\tau^{rad} = 0$), then

$$\Delta\nu_n = \frac{1}{2\pi\tau_j^{rad}},$$

- If $|i>$ is an excited state, then

$$2\pi\Delta\nu_n = \frac{1}{\tau_j^{rad}} + \frac{1}{\tau_i^{rad}} = A_j + A_i.$$

For a metastable state, $\tau^{rad}$ varies from a few $\mu$s up to several minutes. For a resonant state, the radiative lifetime is a few ns. Therefore the natural linewidth of an optical transition is around 1 GHz.

### 2.3.2 Doppler broadening

Let's consider an atom moving at velocity $\mathbf{v}$ with respect to an observer at rest relative to the medium. The absorption frequency of the atom for a plane electromagnetic wave with wave vector $\mathbf{k}$ is shifted due to the Doppler effect. The wave frequency $\nu$ in the stationary reference frame is modified in the frame of the moving atom:

$$\nu' = \nu - \frac{\mathbf{k}\cdot\mathbf{v}}{2\pi}. \tag{6}$$

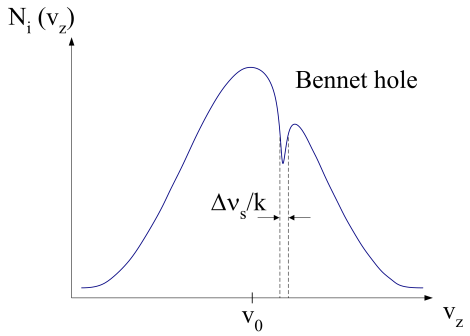


**Figure 2: Bennet hole in the VDF in saturation regime.**

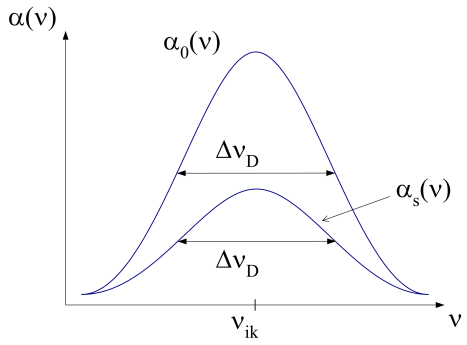


**Figure 3: Saturated Doppler line profile.**

The wave interacts with the atom only if $\nu'$ corresponds to the optical transition frequency $\nu_0$:

$$\nu = \nu_0 + \frac{\mathbf{k}\cdot\mathbf{v}}{2\pi} \rightarrow \Delta\nu = \nu - \nu_0 = \frac{\mathbf{k}\cdot\mathbf{v}}{2\pi}. \tag{7}$$

The quantity $\Delta\nu$ is termed the Doppler shift of the transition. When $\Delta\nu > 0$, the atom and the wave propagate in the same direction: The absorption frequency increases and the transition is blue shifted. When $\Delta\nu < 0$, the atom and the wave propagate in opposite directions: The absorption frequency decreases and the transition is red shifted.

The Doppler broadening is the broadening of a spectral line due to the Doppler effect caused by the distribution of velocities of atoms. Different velocities result in different shifts, the cumulative effect of which is the line broadening. When the Doppler broadening originates in the thermal motion of the atoms, the absorption line profile is Gaussian. The mean atom velocity is inferred from the shift of the line center. The temperature $T$ is obtained from the full width at half maximum $\Delta\nu_D$ of the profile:

$$\Delta\nu_D = \frac{\nu_0}{c}\sqrt{\frac{8\ln(2)k_BT}{m}}, \tag{8}$$

where $c$ is the speed of light in vacuum, $k_B$ the Boltzman constant and $m$ the atomic mass.

When the medium departs from thermodynamic equilibrium, the profile is not Gaussian anymore and it can have any shape. The mean velocity is then determined from the first order moment and the temperature is obtained from the second order moment using the relation $m\sigma^2 = k_BT$, where $\sigma$ is the standard deviation.

**Voigt profile**

The profile of an optical transition between two energy levels in fact corresponds to the convolution product between the Lorentzian natural profile and the Gaussian Doppler profile (in equilibrium). The result is a Voigt function that can only be computed numerically [9]. However, in most cases $\Delta\nu_D \gg \Delta\nu_n$, and the measured line profile is Gaussian.

### 2.3.3 Other broadening mechanisms

There are other line broadening mechanisms that can be encountered during LIF spectroscopy experiments [9]:

- Time of flight broadening: It originates in the finite interaction time between the atom and the wave,

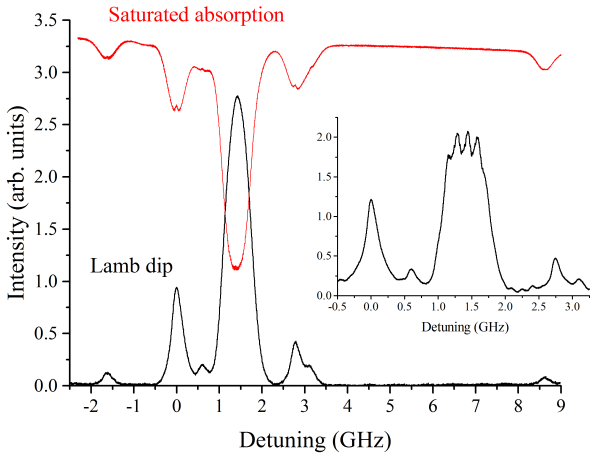


**Figure 4: Structure of the $6s'[0\frac{1}{2}]_1 \rightarrow 6p'[1\frac{1}{2}]_2$ transition of the Xe atom at 834.68 nm. Top: Absorption signal on the probe beam with Lamb dips. Bottom and insert: Lamb dips obtained when modulating the pump beam and using phase-sensitive detection [25].**

- Pressure broadening: Due to a shift of energy levels during a collision event,
- Stark broadening: Due to collisions with charged particles, especially electrons,
- Power broadening: When the pumping rate induced by the laser beam is larger than the relaxation rate of the transition, see section 2.4.

## 2.4 Saturation: Lamb dip

The Lorentzian natural absorption profile $\alpha(\nu)$ can be written in the form [9, 11]:

$$\alpha(\nu) \propto \frac{1}{(\nu - \nu_{ij})^2 + (\frac{1}{2}\Delta\nu_n\sqrt{1+S})^2}, \tag{9}$$

where $\nu_{ij}$ refers to the line center frequency and $S$ is the saturation parameter. The latter reads

$$S = \frac{\rho(\nu)B_{\mathrm{ij}}}{R}, \tag{10}$$

where $\rho$ is the spectral energy density in J m$^{-3}$ s, $B_{\mathrm{ij}}$ is the Einstein coefficient for photo-absorption in m$^3$ J$^{-1}$ s$^{-2}$ and $R$ in s$^{-1}$ is the total relaxation rate of the transition that accounts for radiative and collision processes. $S$ is therefore the ratio of the optical pumping rate to the relaxation rate of the system. When the laser energy is large, $S > 1$ and the absorption process becomes non linear. The fluorescence signal decreases and the line profile broadens. At extreme laser energy, the transition is fully saturated and the medium is transparent for the incident light.

As most EP devices rest on a low-pressure discharge for which Doppler broadening dominates, it is of relevance to examine the effect of saturation on a Gaussian profile. At high laser intensity, the lower energy level $|i>$ is strongly depopulated around the laser frequency $\nu$. In other words, the atomic VDF is depopulated

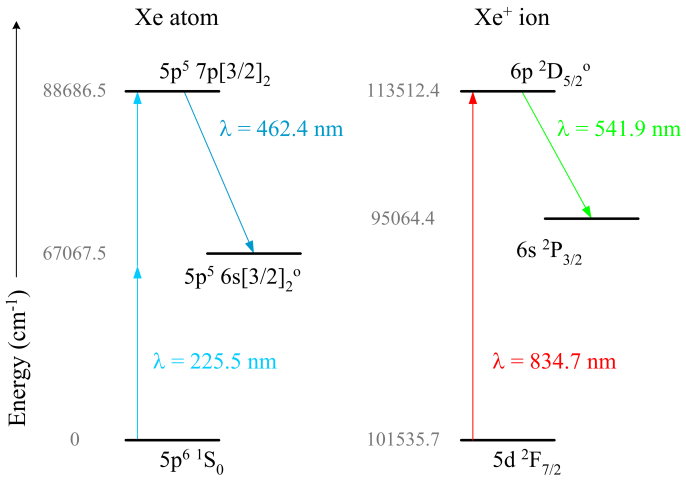


**Figure 5: TALIF energy diagram for detection of the ground-state Xe atom (left) and single-photon LIF energy diagram for probing a metastable state of the $Xe^+$ ion (right). Wavelength values are given in air.**

around the velocity $v$ that accounts for the Doppler shift, as can be seen in Figure 2. In fact a hole is created in the VDF, the so-called Bennet hole [9], whose width is $2\pi\Delta\nu_{n,\mathrm{sat}}/k$, where $\Delta\nu_{n,\mathrm{sat}} = \Delta\nu_n\sqrt{1+S}$ is the saturated natural linewidth and $k$ is the wave vector magnitude. The hole cannot be directly detected when scanning the laser frequency across the line profile. The consequence of continuous hole formation is a decrease in the absorption as exemplified in Figure 3. If the profile is purely Gaussian, there is no broadening. The latter is only observed when the Lorentzian natural profile prevails, i.e. when the laser power is very high.

The Bennet hole can be detected using two laser beams: a first one at high power – the pump beam – saturates the transition and creates the hole and a second one set at low power not to saturate the transition – the probe beam – scans the absorption profile. Another possibility is to use two counterpropagating laser beams coming from the same intial beam with wave vector +**k** and -**k**. A hole is then detected at the center of the line: The Lamb dip [9, 25]. Laser spectroscopy in saturation regime allows a great gain in spectral resolution as the latter is not limited anymore by the Doppler effect but solely by the Lamb dip width assuming an infinitely narrow laser profile and no dispersion in the wave vectors. Doppler-free LIF spectroscopy in pump-probe beam configuration has for instance been used to determine the hyperfine structure and the isotopic shifts of several Xe atom and Xe singly-charged ion lines in the near-infrared [25]. Figure 4 displays the Lamb dip in the absorption spectrum of the Xe atom transition at 834.68 nm. The Lamb dip width is much smaller than the Doppler width as shown in the upper trace.

## 2.5 Multi-photon excitation process

In paragraph 2.1, we only considered absorption of a single photon to excite an optical transition between two quantum levels. However, due to the large energy spacing involved, the detection of ground-state atoms or molecules often requires the use of highly energetic photons in the VUV or XUV domain of the electromagnetic spectrum of which generation is experimentally demanding [12, 22]. The problems connected with single-photon excitation can be avoided with the application of a two-photon excitation scheme. This non-linear optical technique is then called Two-Photon Absorption Laser Induced Fluorescence or TALIF in short [9, 12, 13, 26, 27]. Notice the quantum mechanics selection rules for a two-photon transition differ from the ones

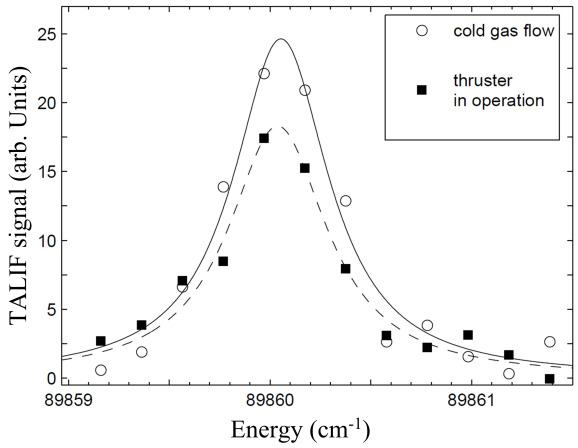


**Figure 6: Spectral profile after two-photon excitation of the Xe atom ground-state at 225 nm in the downstream region of the RIT-10 thruster ion beam [31].**

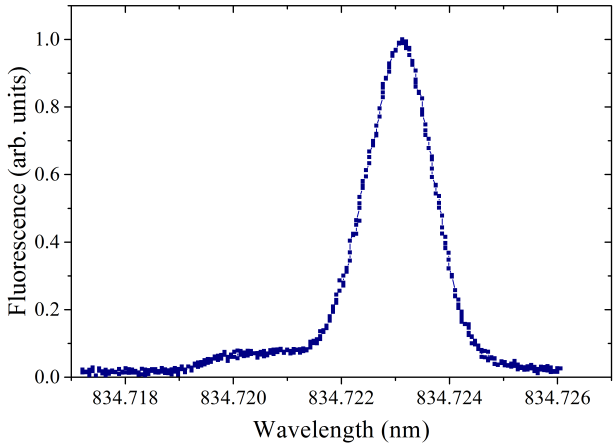


**Figure 7: Spectral profile after excitation of a $Xe^+$ ion metastable state with near IR photons during LIF experiments on Hall thrusters [17].**

associated with a single-photon transition [28, 29] .

The theoretical calculation of the fluorescence yields that results from a two-photon excitation can be found elsewhere [26, 27]. We here only propose a rapid and simplified description of the calculation in the case of an unsaturated two-photon excitation for which a rate equation description is justified. The effect of the laser intensity on the ground-state population $N_i$ can be described by a differential equation very similar to equation 1

$$\frac{d}{dt}N_i(t) = -W(t)N_i(t), \tag{11}$$

where $W(t)$ is the two-photon excitation rate which is expressed with the aid of the generalized two-photon excitation cross-section $\sigma^{(2)}$

$$W(t) = G^{(2)}\sigma^{(2)}g(\nu)\left(\frac{\hat{I}(t)}{h\nu}\right)^2, \tag{12}$$

where $\nu$ is the photon frequency, $\hat{I}(t)$ is the mean laser pulse power per unit area in $\mathrm{W\,m^{-2}}$, $g(\nu)$ in s describes the normalized profile of the two-photon transition which is the convolution of the laser line profile and atomic absorption line profile, and $G^{(2)}$ is the two-photon statistical factor [30]. If the loss of population due to photo-ionization and amplified-stimulated emission is neglected, the total amount of fluorescence photons $n_{\mathrm{fluo}}$ detected at the laser frequency $\nu$ is

$$n_{\mathrm{fluo}} = KG^{(2)}N_i(0)\frac{A_{jk}}{A_j + Q_j}\sigma^{(2)}g(\nu)\frac{\hat{I}^2}{(h\nu)^2}, \tag{13}$$

where $K$ is an experimental factor that accounts for all components of the detection system. The fluorescence signal is therefore proportional to the initial ground-state population and to the square of the laser pulse energy.

Figure 5 shows a LIF energy diagram for the Xe atom in the ground-state and for the $Xe^+$ ion in a metastable state. Detection of Xe atoms is performed by TALIF spectroscopy with two 225.4 nm photons whereas detection of metastable $Xe^+$ ions is achieved by single-photon LIF at 834.7 nm. The two-photon scheme in the VUV has been used to measure the Xe atom density in the beam of radio-frequency ion engines [31–33]. The

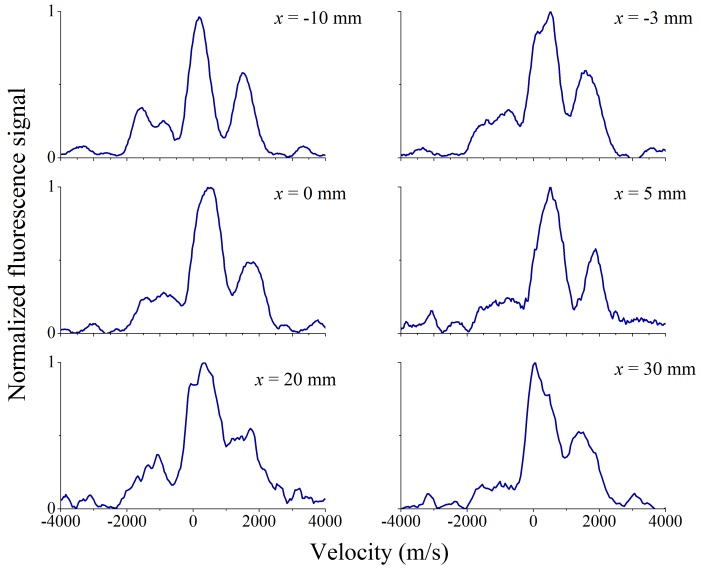


**Figure 8: Series of line profiles of the 823.2 nm line connected with the Xe atom metastable $1s_5$ level. Measurements were taken on the channel axis of the SPT100-ML Hall thruster [34]. $x = 0$ refers to the channel exit plane.**

one-photon scheme in the near infrared is often used to obtain the $Xe^+$ ion VDF in the discharge and in the plume of Hall thrusters [17].

## 2.6 Examples of fluorescence lineshapes

The next three figures are examples of fluorescence lineshapes measured in the plasma of electric propulsion devices.

The Xe atom spectrum in Figure 6 has been obtained by TALIF at 225 nm downstream the acceleration grid of the RIT-10 ion engine [31]. The LIF setup is based on a tunable pulsed Nd:YAG pumped dye laser. The dye laser output is frequency doubled with a BBO crystal to generate UV light. The fluorescence lineshape mostly images here the laser line profile. The absolute ground-state Xe atom number density can nevertheless be inferred from integration of the line shape after calibration of the LIF signal.

Figure 7 shows the fluorescence lineshape after excitation of a $Xe^+$ ion metastable state using the near-infrared LIF scheme in Figure 5. The signal was obtained in a low-pressure RF reference cell with a cw laser diode prior LIF experiments in a Hall thruster [17, 35]. The lineshape is the sum of 19 hyperfine and isotopic components due to the existence of 9 stable Xe isotopes [25].

A series of normalized lineshapes that correspond to the $1s_5 \rightarrow 2p_5$ transition of the Xe atom at 823.2 nm is displayed in Figure 8. LIF spectra were recorded at several axial positions along the channel centerline of the SPT100-ML Hall thruster [25]. The complicated lineshape results from the isotopic shifts and the hyperfine structure of the transition. Frequency were converted into velocity to directly monitor the Doppler shift. The atom mean velocity varies in the course of the flow, due to a combination of several phenomena, see [34]. Another interesting point is the fact that the overall shape of the profile changes. It is a direct consequence of the presence of a strong magnetic field at the thruster exit plane. A static magnetic field produces a splitting of a transition into several components: the Zeeman splitting [9, 18, 19]. The Zeeman effect must be accounted for

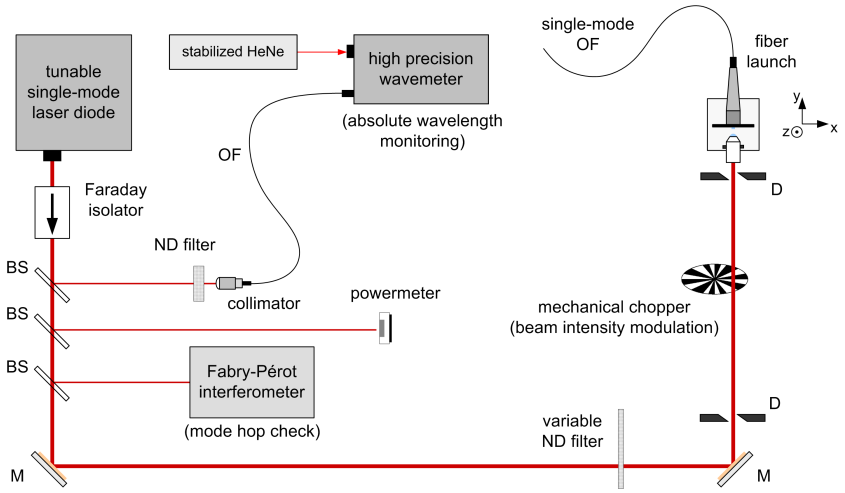


**Figure 9: Diagram of a continuous-wave LIF optical train based on an amplified laser diode (BS: beam splitter, ND: neutral density, M: mirror, D: diaphragm, OF: optical fiber).**

when computing the undisturbed lineshape in order to accurately extract the velocity and the temperature [34, 36]. Since the energy gap between the Zeeman sub-levels is a function of the magnetic field, this effect can also be used to measure the magnetic field magnitude [36].

## 3.0 EXPERIMENTAL ARRANGEMENT

### 3.1 Optical train

Several configurations of a LIF or a TALIF optical bench can be found depending on laser type, laser beam injection system, collection optics and detection system, see e.g. [11–17, 22, 25–27] and references herein. As an example we describe here the optical bench available in our team for time-averaged and time-resolved LIF experiments on Hall thruster discharge and plume [17]. The laser beam used to excite metastable and resonant levels of atoms and ions is produced by an amplified tunable single-mode external cavity laser diode that can deliver up to 700 mW of power in the 810-840 nm spectral domain. The laser remains mode-hop free over a frequency tuning range of more than 10 GHz. The spectral width of the laser beam profile is about 1 MHz. Behind the tapered amplifier the laser beam passes through a Faraday isolator to prevent optical feedback into the laser cavity. The wavelength is accurately measured by means of a calibrated wavemeter whose absolute accuracy is 80 MHz ($\approx$ 60 m/s). Calibration of the wavelength can also be performed with a $NO_2$ absorption cell or with a reference plasma cell with atoms at rest. A scanning confocal Fabry-Pérot interferometer with a 1 GHz free spectral range is used to real-time check the quality of the laser mode and to detect mode hops. The power of the beam is also continuously monitored. The primary laser beam intensity is modulated by a mechanical chopper at a frequency $\sim$ 1 kHz before being coupled into a single-mode optical fiber of 5 $\mu$m core diameter. The fiber carries the beam into the vacuum chamber. A schematic of the optical bench is depicted in Figure 9. Modulation of the laser beam can also be achieved with an acousto-optic modulator (AOM) or with an electro-optic modulator (EOM). High-reflectivity mirrors can be used instead of an optical fiber to transport the laser light.

Several laser injection schemes are possible according to the velocity component of interest [17]. The laser beam can be shined from the back of the source through a dedicated orifice to monitor the axial velocity

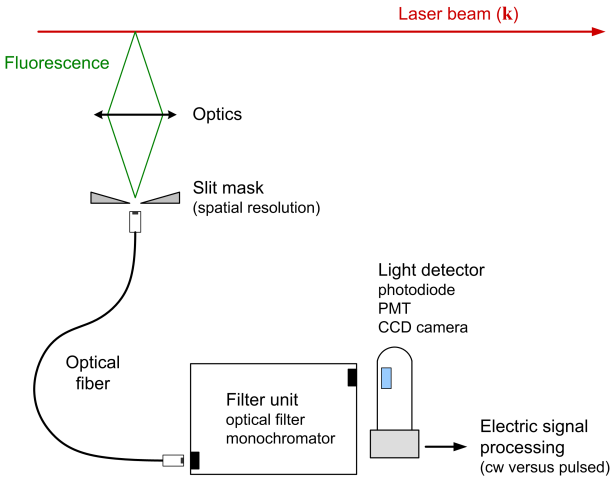


**Figure 10: Organization of the main components of an optical detection branch for a LIF setup.**

component. Another possibility is to shine the laser beam from the front. In that case some optical components are introduced into the ion beam. The laser beam can also propagate in the vertical or horizontal plane to access the radial or the azimuthal velocity component. An optical fiber with a collimator or a set of mirrors can be used inside the vacuum chamber to guide the laser beam and to focus it in the region to be probed. Power deposition in the measurement volume must be well controlled in order to warrant a weak saturation effect of the studied transition.

## 3.2 Detection branch

A layout of a generic detection branch for a LIF experimental setup that incorporates the main components is depicted in Figure 10. In our case, light detection is realized by way of a 25 mm in diameter 40 mm focal length bi-convex quartz lens, which focuses the fluorescence light onto a 200 $\mu$m core diameter optical fiber. The lens holder is mounted onto a travel stage that moves parallel to the laser beam **k** vector to allow for measurements at several positions. The magnification ratio is 1 meaning that the spatial resolution is 200 $\mu$m. In order to probe the interior of the channel, two approaches are possible. A several mm in length slit can be made in the channel dielectric outer wall to look inside the channel. Another way involves orienting the collection optics at an oblique angle relative to the laser direction. The latter solution is preferred as no modification of the thruster design is required. The fluorescence light transported by the 200 $\mu$m fiber is focused onto the entrance slit of a 20 cm focal length monochromator that isolates the fluorescence line from the rest of the spectrum. A narrow-bandwidth interference filter can be used instead. A photomultiplier tube with a maximum quantum efficiency is the visible range and a low dark noise level serves as a light detector. A CCD camera is not necessary as the measurement is one-dimensional. A photodiode can also be used as photodetector as it is a low cost device with a high quantum efficiency and a long lifetime. The gain is however weak, the collection area is small and the overall sensitivity is low. For time-averaged LIF measurements, a lock-in amplifier operating at the chopper frequency is used to discriminate the fluorescence light from the intrinsic plasma emission. When a pulsed laser is used, the florescence decay temporal profile can be recorded with e.g. a fast oscilloscope. The PMT output can also be connected to a boxcar averager, also termed gated integrator, to measure the LIF signal intensity. Scanning of the laser cavity, data acquisition and laser wavelength monitoring must of course be computer controlled.

Notice the optogalvanic effect can be used to detect absorption of the laser light and to construct the absorption profile of an optical transition [37]. The optogalvanic effect is the change in the conductivity of a gas discharge induced by light on resonance with an atomic transition. The change in conductivity translates into a change in current that can be easily measured.

The experimental $K$ factor encountered in Equations 5 and 13 is directly linked to the detection branch. $K$ can be written as:

$$K = V \frac{\Omega}{4\pi} T \eta G, \tag{14}$$

where $V$ is the detection volume, $\Omega$ is the solid angle of the collection optics, $T$ is the transmission of all components of the detection branch (lenses, fibers, mirrors, windows, monochromator or filter, detector window), $\eta$ is the light detector quantum efficiency and $G$ accounts for the detector gain and amplifier sensitivity. The accurate experimental measurement of the $K$ factor is very difficult. A calibration procedure is therefore preferable to cancel it. The $K$ factor must be as high as possible to guarantee a large fluorescence signal level. Large optics with a high transmission at the fluorescence wavelength are therefore required. The light detector characteristics are also of relevance.

### 3.3 2D and 3D LIF

The velocity of the probe species is measured in the direction of the laser beam, i.e. in the wave vector **k** direction. We have considered so far LIF experiments with a single laser beam wherein only one component of the particle velocity vector is interrogated. Naturally combination of laser injection geometries are possible to offer multi-dimensional LIF diagnostics [14, 38]. If a cylindrical symmetry is assumed or if the physical phenomena at stake are two-dimensional, two laser beams are usually sufficient. 3D LIF is of course possible with the use of 3 beams or more. In some complicated situations, 3 beams are not sufficient to capture all the information about the VDF and one must turn towards LIF tomography in phase space, see e.g. references [39–41]. The laser beams should be shined simultaneously to ensure the velocity components are linked to the same processes. This is especially critical for unstable, unsteady or pulsed plasma discharges.

The experimental arrangement for multi-dimensional LIF is the following. A laser beam is splitted into 2 or 3 secondary beams by way of beam splitters each with the same light intensity. If necessary the polarization must be maintained. Subsequently the intensity of each beam is modulated at a different frequency. The beams are directed into the plasma and they interact in the measurement volume. Optics collect the light and guide it to a photodetector. A multi-mode optical fiber or a fiber bundle can be employed to guide the light. The light passes through a narrow bandwidth interference filter or a monochromator before being focused onto the photodetector of which the electrical output is divided among 2 or 3 lock-in amplifiers, each tuned to one of the modulator frequencies. This scheme allows the simultaneous measurements of components of the atom or ion velocity distribution function.

The velocity vector field was determined in the plume near-field of several high and low power Hall thrusters by means of 2D LIF, see [17] and references herein. The local ion velocity can be assumed to correspond to either the mean or the most probable velocity. In the case of 2D-LIF measurements on Hall thrusters and variants, one therefore obtains the transverse (radial) and longitudinal (axial) velocity components from which the ion velocity vector can be constructed assuming a cylindrical symmetry. Huang and co-workers have reconstructed the velocity vector inside the channel of the 6 kW-class H6 Hall thruster applying cw LIF in the near IR on metastable $Xe^+$ ions [42]. They have shown that the vectors point towards the surface nearby walls. Their results have major implications for the channel wall erosion studies. Figure 11 shows the $Xe^+$ ion velocity vector field in the channel of the high-power H6 Hall thruster operating at 600 V and 10 mg/s.

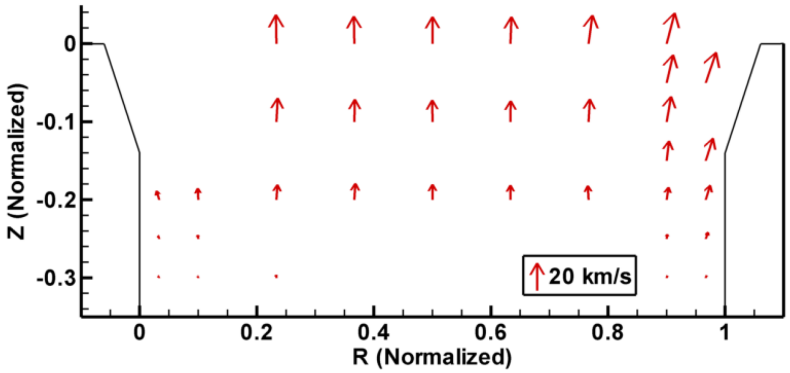


**Figure 11: $Xe^+$ ion velocity vector plot in the channel of the high-power H6 Hall thruster operating at 600 V and 10 mg/s in xenon, after [42]. A reference vector is included to show the length of a 20 km/s vector..**

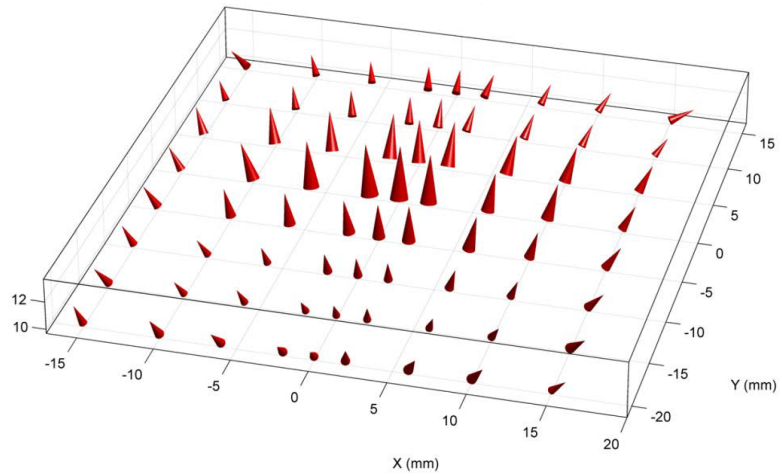


**Figure 12: Plot of the Cs atom velocity vector field in the plume of a cesium-fed FEEP thruster, after [43]. Under the FEEP operating conditions, the thrust level was 30 $\mu$N and the emitter temperature was 35°.**

Three-dimensional LIF has been applied to investigate the neutral cesium flow rate in the plume of a cesium-fed Field Emission Electric Propulsion (FEEP) thruster [43]. 3D LIF was performed with a tunable laser diode on hyperfine components of the D2 transition of the cesium atom at 852 nm. Figure 12 shows the Cs atom velocity vector field in the plume of the FEEP thruster [43]. The thruster emitter temperature was 35° and the thrust level was 30 $\mu$N. The velocity vector plot images the neutral atom plume divergence. In this study, the absolute number density of Cs atoms was also measured. Combining the density data with the velocity data authors were able to calculate the neutral mass flow rate.

## 4.0 MEASURED QUANTITIES

### 4.1 Velocity distribution function

In many electric propulsion plasma sources the fluorescence line shape images to a large extent the probed particle velocity distribution function as the pressure is low, hence collisional broadening can be neglected. The recorded spectral line shape is in fact the convolution between the VDF and the laser frequency profile as we

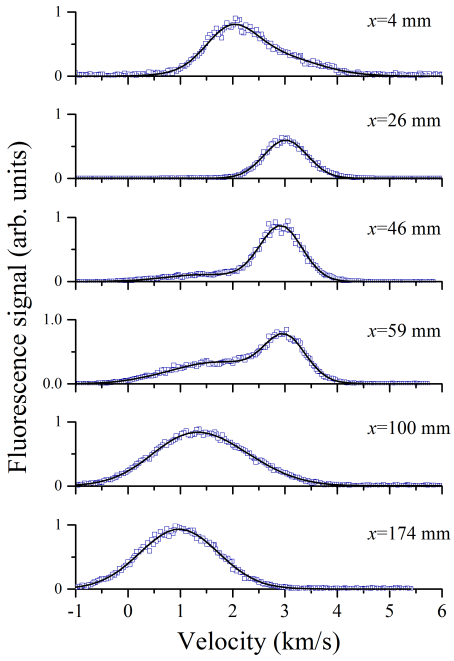


Figure 13: Axial velocity distributions of metastable Ar atoms recorded along the axis of a cascaded arcjet at 20 Pa background pressure [44]. The metastable Ar VDF images the ground-state Ar VDF.

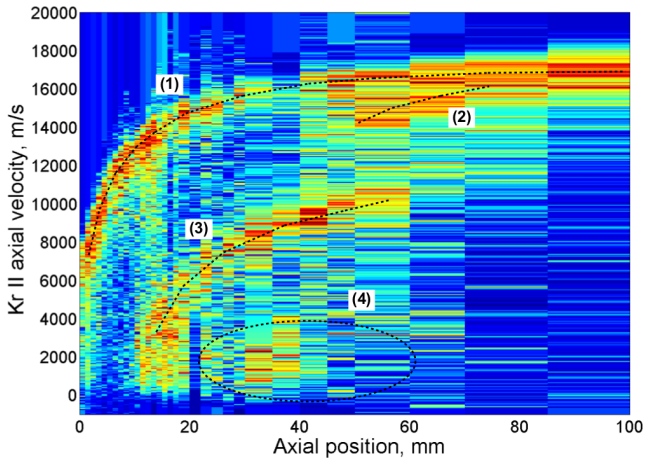


Figure 14: Axial VDF of metastable $Kr^+$ ions measured along the channel axis of the 200 W permanent magnet ISCT200 Hall thruster [45]. Four different ion groups can clearly be identified.

have seen in section 1. Direct access to the VDF therefore requires narrow bandwidth lasers, i.e. cw sources. Although pulsed lasers often prevent accurately measuring the VDF, they allow the determination of the flow velocity and the species concentration. Since obtaining the temperature calls for a deconvolution on recorded line profile, the value is accurate only if the Doppler broadening is large. One can find many examples of atom and ion VDF measurements by way of LIF spectroscopy in the open literature, see e.g. [17] and references herein.

Figure 13 shows metastable Ar atom axial velocity distribution functions recorded at different positions downstream the exit plane of a cascaded arcjet [44]. Measurements were carried out by resonant LIF on the Ar atom $1s_5 \rightarrow 2p_9$ transition at 811.53 nm with a single-mode external cavity diode laser. Although the measured spectra originate from metastable Ar atoms, the measured velocity distributions image the velocity distributions of ground-state Ar atoms [44]. The distributions for $x \leq 20\,\mathrm{mm}$ is distorted due to the existence of an accelerating E-field acting on $Ar^+$ ions. At 20 Pa background presure, for $20 < x < 30$ mm the measured distribution can be described to a good approximation with a Gaussian profile, i.e. the flow is in thermodynamic equilibrium. Behind $x = 30$ mm, i.e. in the shock wave region, the VDF measured along the jet centerline starts to deviate from the equilibrium form. Across the stationary shock wave, the Ar VDF can be decomposed into two Gaussian VDF: one corresponds to the conditions upstream of the shock ("fast" component characterized by a high mean velocity and a low temperature), and the other one corresponds to the conditions in the shock wave ("slow" component characterized by a low mean velocity and a high temperature). Across the shock

wave, the population of the fast Gaussian component is gradually transferred to the slow component by means of collisions. Details about the bimodal approximation for the VDF within a shock wave can be found in [46] and reference herein. Behind the shock region, $x \geq 150$ mm, i.e. in the subsonic region of the expansion, the velocity profile can be described with a single Gaussian again. In this region the flow is in equilibrium and can be described along the jet axis with one mean velocity and one temperature.

Figure 14 shows the contourplot of the normalized Kr II ion axial VDF along the channel axis of the permanent magnet 200 W ISCT200 Hall thruster firing with a discharge voltage of 200 V [45]. Four different ion groups are clearly identified. The main branch labeled (1) corresponds to ions that accelerate from 5000 m/s in the channel exit plane up to 16000 m/s at 100 mm. These ions are created inside the channel and they experience the whole potential drop. The second branch (2) is located where the electric field is too low to accelerate ions to very high velocity. This group corresponds to ions coming from the opposite side of the annular channel and interacting with the main ion beam. The apparent acceleration is a mere geometric effect. It results from the axial velocity component of the divergent velocity ion population. The third branch (3) appears with velocity from 0 m/s at 10 mm up to 10000 m/s at 50 mm. The slow ions originate either from charge exchange collisions between the main beam (1) or the diverging beam (2) and background residual gas or cathode gas, or from local ionization. Slow ions are produced close to the channel exit plane where densities are large. They are subsequently accelerated as the electric field stretches out up to $x = 60$ mm. Beyond 60 mm, the third branch (3) is lost in the background noise. The last group (4) is observed with velocities varying between 0 m/s and 4000 m/s. It corresponds to slow ions that are created at locations too far away from the channel exit plane to be strongly influenced by the electric field. This ion population may result from local ionization or interaction between beam from various part of the channel. There is no significant acceleration and the ions propagate axially at a constant velocity $\approx 1000$ m/s that remains in the range of the ion acoustic velocity. An identical picture is obtained when the ISCT200 thruster is operated with xenon [45].

## 4.2 Particle velocity

The evolution of the Xe II ion mean axial velocity component along the channel axis of the 1.5 kW-class SPT100-ML Hall thruster is displayed in Figure 15. In this experiment the thruster was operated at 250 V and 4.5 mg/s xenon flow rate [47]. The dashed line in Figure 15 corresponds to the ion velocity obtained assuming a full conversion of the potential electrostatic energy into axial kinetic energy. The highest value of the mean ion velocity is close to the theoretical limit, which demonstrates the high energy conversion efficiency, an intrinsic characteristic of a Hall thrusters. The length of the acceleration layer is around 30 mm in this example. The breadth of the acceleration region in a Hall thruster is typically one channel mean radius. The accelerating potential $U_{\rm acc}$ is derived from an energy conservation equation assuming a collisionless medium:

$$\frac{1}{2}mv^2 = eU_{\rm acc}, \tag{15}$$

where $v$ is the ion velocity and $e$ is the elementary charge. The ion velocity can be either the mean velocity or the most probable velocity. The accelerating potential profile along the channel axis of the SPT100-ML thruster is shown in Fig. 15. The potential was computed from the ion mean velocity. A large fraction of the ion acceleration occurs behind the channel exit plane. It is often the case for Hall thrusters, see e.g. [17], although the outside fraction depends on the magnetic field map and on the thruster geometry.

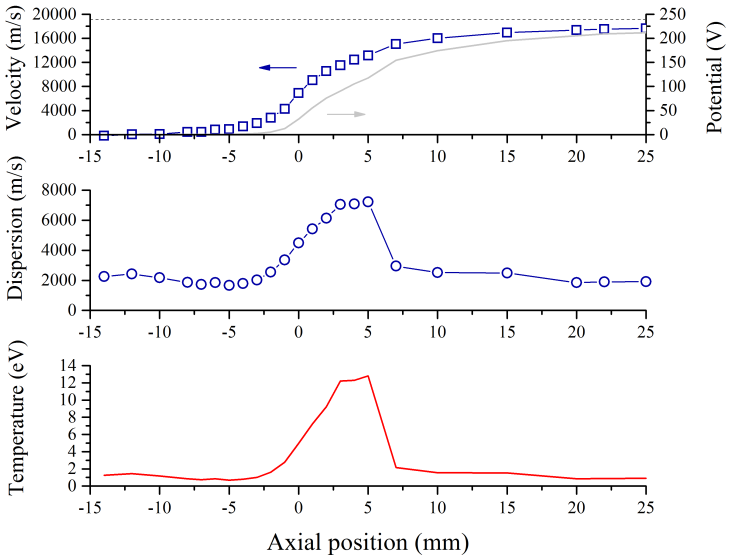


**Figure 15: $Xe^+$ ion mean velocity, accelerating potential, velocity dispersion and temperature as a function of the axial position for the SPT100-ML thruster operating at 250 V [47].** $x = 0$ **indicates the channel exit plane.**

## 4.3 Temperature

The $Xe^+$ ion VDF broadens in the course of the flow as can be seen in Figure 15. The dispersion follows a single-peaked curve. The maximum value is around 7000 m/s. It is reached in the vicinity of the thruster channel exit plane. The large value of the dispersion originates from the interconnection between the ionization and the acceleration regions [17]. The distribution shown in Figure 15 has a shape that is typical for Hall thrusters whatever the input power, the sizes and the propellant: the dispersion first increases slowly up to a maximum value; it then exhibit a sharp decay towards a constant level that is never zero. The magnitude of the velocity dispersion depends upon the thruster operating conditions.

The dispersion of the VDF is related to the Doppler effect, see paragraph 2.3.2. The velocity dispersion can then be converted into temperature. The on-axis temperature distribution of the $Xe^+$ ion in the SPT100-ML thruster discharge is shown in Figure 15. The ion temperature is extremely high in the acceleration region contrary to the atom temperature that is of about 700 K [34]. Notice that in the plume the ion temperature is still around 1 eV much higher than the backgournd gas temperature, typically around 300 K.

## 4.4 Density

As we have seen in section 2.0, the area of the fluorescence line profile is proportional to the density of the particle in the probed level $|i>$. However, the determination of an absolute number density requires to calibrate the LIF signal. The fluorescence light that originates from pumping of an excited metastable or resonant state is impossible to accurately calibrate. In that case only relative number density can be obtained. The fluorescence radiation generated from LIF on ground-state atoms or molecules can be calibrated by various means, see paragraph 2.2, in such a way an absolute density can be given. The case of ground-state ions is not as straightforward. One possible approach consists of combining LIF and electrostatic probe measurements at the same location. The local electron density inferred from the probe IV curve can serve to calibrate the fluorescence line shape, assuming quasi-neutrality.

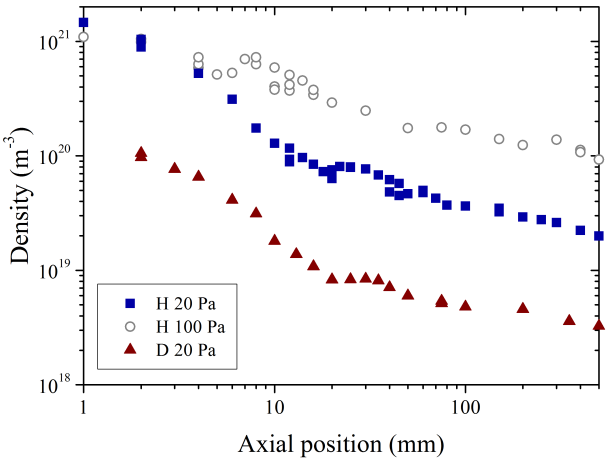


**Figure 16: Ground-state H and D atom absolute density profile along the jet centerline of a cascaded arcjet [48]. The atoms were probed by TALIF at 205 nm.**

Figure 16 shows the ground-state hydrogen and deuterium atom absolute density profile along the jet centerline of a cascaded arcjet operating with pure $H_2$ [48]. The H and D atoms were probed by means of TALIF at 205 nm with detection of the resulting fluorescence yield on the Balmer-$\alpha$ line at 656 nm. Calibration was performed via a two-photon excitation scheme on a known amount of krypton. In Figure 16, there is no evidence of any density jump throughout the stationary shock wave in the downstream jet region. The H and D atom density profiles reveal a non-conservation of the atom forward flux throughout the stationary shock wave in contradiction with the well established Rankine-Hugoniot relations. Behind the shock wave, the density decreases, and since the temperature also decreases, hydrogen and deuterium atoms do not flow at constant static pressure which is a sign for losses.

## 5.0 ELECTRIC FIELD DETERMINATION

### 5.1 Indirect way: Using the VDF

The electric field distribution is afundamental quantity to understand the physics of electric space propulsion devices. It can be inferred indirectly from the ion velocity distribution function measured by LIF spectroscopy following various approaches [17, 49]. A first possibility is to derive the field from the most probable velocity using the energy conservation equation for a collisionless plasma medium. Using the ion mean velocity (first order moment of the VDF) results in an underestimation of the true local axial electric field magnitude. The electric field in axial direction $E_x$ is the derivative of the acceleration potential distribution, the latter being directly linked to the velocity profile as we have seen. The $E_x$ field therefore reads:

$$|E_x(x)| = \frac{dU_{acc}(x)}{dx} = \frac{m}{e} v(x) \cdot \frac{dv(x)}{dx}. \tag{16}$$

Note that we neglect the mixed spatial derivatives in the preceeding calculation [49].

A second approach is based on the fluid equations. Starting from the steady-state continuity and momentum conservation equations for unmagnetized ions, in the case of negligible charge-exchange and momentum

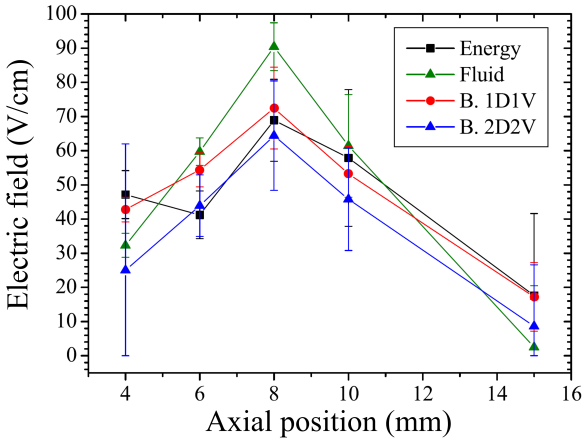


**Figure 17: Calculation of the axial component of the electric field on the channel axis of the ISCT200 Hall thruster using several methods: energy conservation, fluid equations, Boltzmann 1D1V and 2D2V models [49].**

exchange collisions, one can derive an expression for the axial and radial components of the electric field. The atom velocity is also neglected in the calculation. Nevertheless, the plasma density, the ionization frequency and the pressure gradient terms need to be considered for computing the electric field profile using a fluid approach [49].

A last method, which relies on high-order moments of the Boltzmann's equation, has been developed for evaluating the spatial profile of the electric field as well as the distribution of the ionization frequency directly from the measured ion VDF [49–51]. The use of the Boltzmann's equation has several advantages. Firstly, it considers the kinetic nature of the plasma processes and collisions events can be accounted for. Secondly, the ionization and acceleration terms can be evaluated independently. Lastly the measurement of additional quantities is not required. Note that to obtain proper results, the experimental VDFs must be normalized taking into account the laser power, the detector response and the lock-in amplifier settings.

The three methods have been compared with each others in the discharge of the ISCT200 Hall thruster firing at 200 V with xenon [49]. The axial and radial VDF of metastable $Xe^+$ ion have been acquired by means of 2D LIF in the near IR. Outcomes of the three methods are presented in Figure 17. The 1D1V and 2D2V terms refer to the use of the Boltzmann's equation. The 2D2V case accounts for the radial velocity component. The outside peak in the electric field profile is clearly visible and distinguished by all methods. The error bar tends to be larger with the 2D2V model, because of the finite signal-to-noise ratio and numerical errors. The field values are lower with the 2D2V computation since a small fraction of the total energy is lost in the radial component instead of being used for acceleration. The error bars globally tend to widen when the distance from the source increases due to the reduction in the signal-to-noise ratio level. Finally, the fluid model provides acceptable values of the electric field, yet slightly too large, and correctly reveals the field structure.

## 5.2 Direct way: Stark spectroscopy

All methods presented in the previous section are indirect in the sense that they rest upon measurements of the ion VDF and several assumptions to determine the electric field. There is, however, a direct way for extracting the electric field in plasma discharges based on the Stark effect. The Stark effect is the shifting and splitting of spectral lines of atoms and molecules due to presence of an external electric field [9, 10, 18, 19]. The amount of splitting or shifting is called the Stark splitting or Stark shift. The Stark effect is also responsible for the

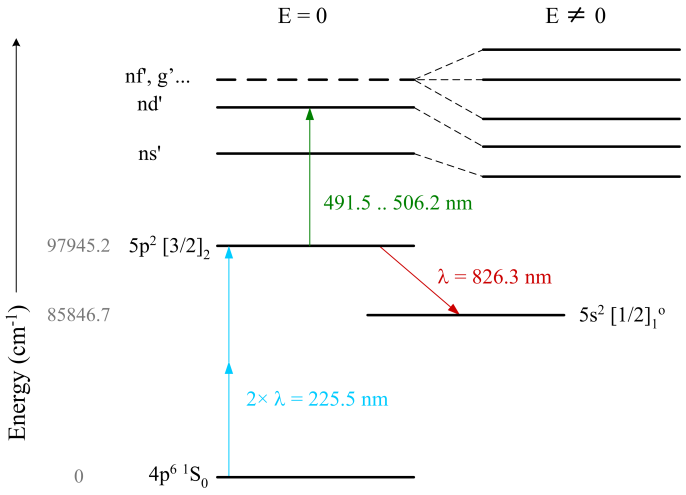


**Figure 18: Energy diagram for fluorescence-dip Stark spectroscopy on krypton. The fluorescence light at 826 nm decreases when the second step excitation is resonant with a (Stark-split) Rydberg state, after [52].**

broadening of spectral lines by charged particles, the so-called Stark broadening. Notice the Stark effect is the electric analogue of the Zeeman effect where a spectral line is split into several components due to the presence of a magnetic field.

Atoms and molecules can serve as probes for electric field measurements. In highly excited Rydberg states, close to the ionization limit, electrons are on large orbits and the effect of the nucleus electric field is relatively weak. Therefore, small external fields can alter the electron trajectories and energy levels are shifted and mixed. The Stark effect increases with the principle quantum number $n$ approximately like $n^2$. Laser spectroscopy allows to measure the line shifts and the amplitude of usually forbidden transitions with high accuracy and high sensitivity [53].

Laser spectroscopic techniques for the measurement of the Stark effect in plasmas can be divided into two groups: optogalvanic detection and fluorescence detection. In optogalvanic detection, atoms or molecules are excited to high Rydberg states, which are easily ionized by collisions. With a pulsed laser system, the change in plasma conductivity generates a short AC signal that is maximum at resonance. The electric field is inferred by measuring the detailed spectrum of a particular transition [54]. Fluorescence radiation emitted from a Rydberg state can also be monitored directly after the laser pulse excitation [52, 55–57]. The LIF technique provides the advantage of high spatial and temporal resolution. Stark spectroscopy has been applied succesfully on H, He, Ne, Ar, Kr and Xe atoms and various diatomic molecules and electric field magnitudes as low as a few V/cm have been measured.

Laser excitation of high Rydberg states is a general problem whatever the applied technique. Due to the large energy gap, direct excitation from the ground-state requires VUV or XUV photons. Direct excitation from a metastable state is one possible approach in a plasma discharge. Alternatively, an intermediate state can also be populated temporarily from the ground state by a two-photon process. In that case, one must turn towards a 2+1 LIF technique: 2 photons in the deep UV range transfer the population from the ground-state to an excited state that is immediatley excited to a high Rydberg state with another photon in the visible or near IR. Besides, a 2-photon scheme with two counter propagating UV beams allows Doppler-free excitation, which greatly improves the accuracy and sensitivity of the technique.

The main limitation of LIF spectroscopy for measuring electric field is the long lifetime of Rydberg states,

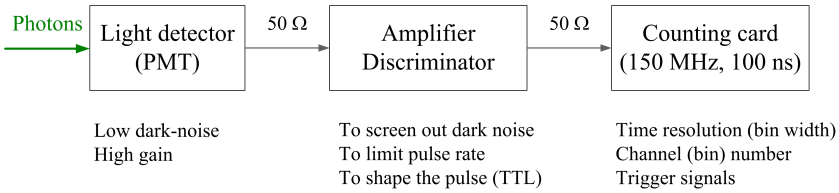


**Figure 19: Photon counting measurement chain block diagram. Photons are converted into electric pulses by the PMT. Pulses are then amplified and selected according to their amplitude (LIF photon versus detector noise). The counting card accumulates the events over $n$ channels of 100 ns width each. Both laser on and laser off acquisitions are performed to reveal the time-dependent LIF signal.**

which prevents using a very high quantum number $n$. This drawback can be circumvent by applying the fluorescence-dip spectroscopy [52, 53]. The principle of the method is depicted in Figure 18 for krypton. In short, the idea is to monitor the fluorescence of the intermediate state in a 2+1 scheme instead of the fluorescence from the probed Rydberg state. When sweeping the frequency of the second laser, the various resonances then correspond to dips in the fluorescence spectrum of the intermediate state. As a consequence the observed signal does not depend anymore on the lifetime of the Rydberg state. With ns laser pulses and energies up to a few mJ, Rydberg states up to $n = 50$ have been observed.

## 6.0 TIME-RESOLVED LIF SPECTROSCOPY

### 6.1 Methods

So far, only time-averaged LIF measurements have been discussed in this contribution. Time-resolved LIF spectroscopy is naturally feasible and applied in many fields, including electric space propulsion. Time-resolved measurements can be achieved either with a pulsed laser or with a continous wave laser although the two ways differ on an experimental viewpoint. When using a nanosecond (ns) pulsed laser, time-resolution is simply achieved by synchronizing the laser pulse with the phenomenon to be studied. The fluorescence light is recorded during and after the laser pulse with a fast PMT connected to a boxcar averager, also named a gated integrator. The gate width must be larger than the LIF decay time. The corresponding background signal, i.e. the natural plasma emission, is recorded with the same settings but without shining the laser. The substraction between the two signals allows to greatly improve the signal-to-noise ratio. Examples of time-resolved LIF measurements using ns lasers in plasmas can be found in references [58, 59]. It is usually not necessary to employ ps or fs lasers when studying low-pressure plasma discharges. The quenching rate being pressure dependent, it stays low in most EP device discharges, therefore the fluorescence radiation decay is governed by radiative processes with a typical duration of a few ns.

Pulsed lasers allow to monitor the change in time of the density as well as of the temperature and velocity when deconvolution with the laser lineshape is feasible. An accurate determination of the time-varying atom or ion VDF however requires the use of a cw laser, as we have seen. Recently, several methods have been developped in the field of EP to measure the time-varying velocity distribution function of ions and atoms in non stationary discharges: pulsed-counting [60–62], heterodyne detection [63], combination of band-pass filtering with phase-sensitive detection [64] and a sample-and-hold technique [65, 66]. All methods share two common points: i) they rest upon the use of a cw laser source and ii) plasma oscillations must exhibit a high temporal coherence, i.e. be quasi periodical. The main difference between the four methods is the way the fluorescence radiation is detected, treated and analysed.

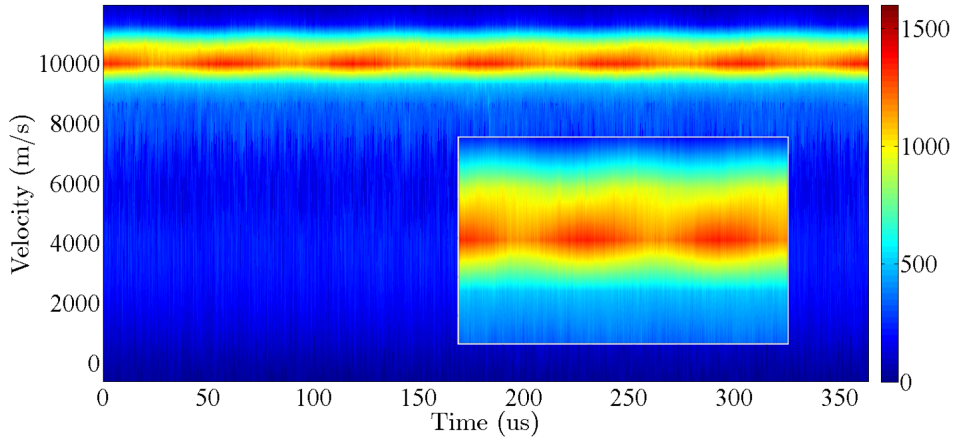


**Figure 20: Temporal evolution of the $Xe^+$ ion VDF 5 mm downstream the ISCT200 Hall thruster exit plane over a few breathing mode oscillation periods. The inset highlights evolution of the most probable velocity groups during the first 150 $\mu$s . The color bar indicates count (LIF photon) number.**

## 6.2 Photon counting

For a very low intensity optical signal, light can be described as a train of discrete photons. When the arrival/detection of photons is well separated in time, the so-called photon counting regime is reached. The typical photon count rate is below a few millions of photons per seconds (Mcps or MHz). Among the four aforementioned cw time-resolved LIF techniques, the photon or pulse counting technique offers the highest sensitivity and the highest temporal resolution.

The photon counting technique has been recently applied to diagnose the oscillating discharge of Hall thrusters [60–62, 67]. The optical bench and the collection optics are similar to the ones described in section 3.0. The measurement chain is schematized in Figure 19. Fluorescence photons are detected by means of a fast high gain low dark noise PMT. A fast amplifier and discriminator module is used to screen out the noise from the PMT. This has two advantages. Firstly, the count rate is limited to avoid the pulse counter saturation. Secondly, any single event is converted into a transistor-transistor logic (TTL) signal. In order to properly adjust the discriminator threshold, events are classified according to their amplitude. Each photon pulse can be distinguished from the background noise by appropriate setting of the discriminator threshold. The pulse counting device is a 150 MHz multichannel scaler. The entire period of the oscillation can be recorded instead of being reconstructed by an external device over several oscillation periods. Moreover, any waveform can be recorded with this technique. A trigger signal starts the acquisition of the incoming photon events over a few oscillations period, which warrants perfect reproducibility for each pass. The channel width (the temporal resolution) is 100 ns. Thousands of passes are necessary to obtain a good LIF signal-to-noise ratio. For each velocity group measurement, the laser wavelength is kept constant through a feedback loop. The LIF signal is extracted through two successive laser on and laser off measurements. The subtraction reveals the fluorescence events collected by the pulse counting device. The statistics is optimized when the substraction is operated after each pass.

Figure 20 shows the contour plot of the temporal $Xe^+$ ion VDF along the channel axis of the 200 W ISCT200 Hall thruster operating at 200 V discharge voltage [60]. Measurements were performed 5 mm downstream the channel exit plane. The HT discharge was stabilized by applying a sinewave voltage on the cathode

keeper. The time-dependent ion VDF is in fact composed of 13 points or velocity groups. This number allows to properly reconstruct the time-averaged VDF. As can be seen in Figure 20, the ion VDF strongly oscillates at the breathing mode frequency ($\sim$15 kHz). The photon counting technique was succesfully applied to investigate the oscillation of the electric field in Hall thrusters at the breathing mode frequency around 10–20 kHz, see [61], as well as at the so-called ion transit time oscillation frequency up to 600 kHz, see [62].

## 7.0 CONCLUSION

This article makes a short review of the Laser-Induced Fluorescence spectroscopy technique applied to EP devices with illustrations showing several measurement outcomes. As shown throughout the entire paper, LIF allows accessing important quantities like the mean velocity, the temperature, the velocity vector and the electric field. For instance, over the past ten years, LIF experiments have allowed significant advances on atomic and ionic transport phenomena in the discharge of Hall thrusters, with consequences on the design and the characteristics.

Finally, to close this article, it is worth mentioning the existence of laser spectroscopy techniques close to the LIF diagnostics, which could find applications in the field of electric propulsion. Laser-collision induced fluorescence (LCIF) is the emission of light from states that have been populated by laser excitation and subsequent collisions. This technique, when combined with a collisional-radiative model, allows to determine the local electron density and temperature within a plasma. Resonance-enhanced multiphoton ionization (REMPI) is a multiphoton absorption process that leads to ionization of the atom or molecule. The resulting charged particles can be detected using an electrostatic probe or microwaves. REMPI is a highly sensitive technique for trace gas monitoring and for the determination of species concentration, at least in gaseous media.

## ACKNOWLEDGMENTS

A large part of the work described in this contribution was carried out in the frame of a joint research program between of CNRS,CNES,SNECMA and Universities entitled "*Propulsion par Plasma dans l'Espace*".

## REFERENCES

[1] Mazouffre, S., "Electric propulsion for satellites and spacecraft: established technologies and novel approaches," *Plasma Sources Sci. Technol.*, Vol. 25, 2016, pp. 033002.

[2] Frisbee, R. H., "Advanced space propulsion for the 21st century," *J. Propulsion Power*, Vol. 19, 2003, pp. 1129–1154.

[3] Jahn, R. G., *Physics of Electric Propulsion*, Mc Graw-Hill, New York, 1968.

[4] Goebel, D. M. and Katz, I., *Fundamentals of Electric Propulsion*, Wiley, Hoboken, NJ, 2008.

[5] Martínez-Sánchez, M. and Pollard, J. E., "Spacecraft electric propulsion – An overview," *J. Propulsion Power*, Vol. 14, 1998, pp. 688–699.

[6] Charles, C., "Plasmas for spacecraft propulsion," *J. Phys. D: Appl. Phys.*, Vol. 42, 2009, pp. 163001.

[7] Ahedo, E., "Plasmas for space propulsion," *Plasma Phys. Control. Fusion*, Vol. 53, 2011, pp. 124037.

[8] Garrigues, L. and Coche, P., "Electric propulsion: comparison between different concepts," *Plasma Phys. Control. Fusion*, Vol. 53, 2011, pp. 124011.

[9] Demtröder, W., *Laser Spectroscopy: Basic Concepts and Instrumentation*, Springer, Berlin, 1998.

[10] Hollas, J. M., *High Resolution Spectroscopy*, John Wiley & Sons, Inc., New York, 1998.

[11] Sadeghi, N., "Molecular spectroscopy techniques applied for processing plasma diagnostics," *J. Plasma Fusion Res.*, Vol. 80, 2004, pp. 767–776.

[12] Döbele, H. F., Czarnetzki, U., and Goehlich, A., "Diagnostics of atoms by laser spectroscopic methods in plasmas and plasma-wall interaction studies (vacuum ultraviolet and two-photon techniques)," *Plasma Sources Sci. Technol.*, Vol. 9, 2000, pp. 477–491.

[13] Amorim, J., Baravian, G., and Jolly, J., "Laser-induced resonance fluorescence as a diagnostic technique in non-thermal equilibrium plasmas," *J. Phys. D: Appl. Phys.*, Vol. 33, 2000, pp. R51–R65.

[14] Biloiu, I. A., Scime, E. E., and Biloiu, C., "One- and two-dimensional laser induced fluorescence at oblique incidence," *Plasma Sources Sci. Technol.*, Vol. 18, 2009, pp. 025012.

[15] Döbele, H., Mosbach, T., Niemi, K., and von der Gathen, V. S., "Laser-induced fluorescence measurements of absolute atomic densities: concepts and limitations," *Plasma Sources Sci. Technol.*, Vol. 14, 2005, pp. S31–S41.

[16] Mazouffre, S., *Spectroscopie de fluorescence induite par diodes laser : Application au diagnostic des plasmas*, Plasmas Froids : Systèmes d'analyse, Modélisation et Rayonnement, Publications de l'Université de Saint-Etienne, Saint-Etienne, France, 2009, pp. 67–90, in French.

[17] Mazouffre, S., "Laser-induced fluorescence diagnostics of the cross-field discharge of Hall thrusters," *Plasma Sources Sci. Technol.*, Vol. 22, 2013, pp. 013001.

[18] Feynman, R. P., Leighton, R. B., and Sands, M., *The Feynman Lectures on Physics, Volume III: Quantum mechanics*, Addison Wesley, New York, 1971.

[19] Cohen-Tannoudji, C., Diu, B., and Laloe, F., *Quantum Mechanics*, Vol. 1 & 2, Wiley, New York, 1991.

[20] Berman, P. R. and Malinovsky, V. S., *Principles of Laser Spectroscopy and Quantum Optics*, Princeton University Press, Princeton, 2010.

[21] Krames, B., Glenewinkel-Meyer, T., and Meichsner, J., "In situ determination of absolute number densities of nitrogen molecule triplet states in an rf-plasma sheath," *J. Appl. Phys.*, Vol. 89, 2001, pp. 3115–3120.

[22] Vankan, P., Heil, S. B. S., Mazouffre, S., Engeln, R., Schram, D. C., and Döbele, H. F., "A vacuum-UV laser-induced fluorescence experiment for measurement of rotationally and vibrationally excited $H_2$," *Rev. Sci. Instrum.*, Vol. 75, 2004, pp. 996–999.

[23] Träger, F., *Springer Handbook of Lasers and Optics*, Springer-Verlag, Berlin, Heidelberg, 2012.

[24] Renk, K. F., *Basics of Laser Physics*, Springer-Verlag, Berlin, Heidelberg, 2012.

[25] Pawelec, E., Mazouffre, S., and Sadeghi, N., "Hyperfine structure of some near-infrared Xe I and Xe II lines," *Spectrochimica Acta Part B*, Vol. 66, 2011, pp. 470–475.

[26] Boogaarts, M. G. H., Mazouffre, S., Brinkman, G. J., van der Heijden, H. W. P., P.Vankan, van der Mullen, J. A. M., Schram, D. C., and Doöbele, H. F., "Quantitative two-photon laser-induced fluorescence measurements of atomic hydrogen densities, temperatures, and velocities in an expanding thermal plasma," *Rev. Sci. Instrum.*, Vol. 73, 2002, pp. 73–86.

[27] Czarnetzki, U., Miyazaki, K., Kajiwara, T., Muraoka, K., Maeda, M., and Döbele, H. F., "Comparison of various two-photon excitation schemes for laser-induced fluorescence spectroscopy in atomic hydrogen," *J. Opt. Soc. Am. B*, Vol. 11, 1994, pp. 2155–2162.

[28] Bonin, K. D. and McIlrath, T. J., "Two-photon electric-dipole selection rules," *J. Opt. Soc. Am. B*, Vol. 1, 1984, pp. 52–55.

[29] Tung, J. H., Tang, A. Z., Salamo, G. J., and Chan, F. T., "Two-photon absorption of atomic hydrogen from two light beams," *J. Opt. Soc. Am. B*, Vol. 3, 1986, pp. 837–848.

[30] Loudon, R., *The Quantum Theory of Light*, Clarendon Press, Oxford, 1983.

[31] C. Eichhorn, S. L., Fasoulas, S., Leiter, H., and Auweter-Kurtz, M., "Two-photon spectroscopy on neutral xenon in the plume of the radio-frequency ion thruster RIT-10," *Proceedings of the 32nd International Electric Propulsion Conference*, IEPC paper 2011–302, Wiesbaden, Germany, 2011.

[32] Crofton, M., "Measurement of neutral xenon density profile in an ion thruster plume," *Proceedings of the 27th Plasma Dynamics and Lasers Conference*, AIAA paper 1996–2290, New Orleans, LA, 1996.

[33] Winter, M. W., Auweter-Kurtz, M., Pfrommer, T., and Semenova, N., "Plasma diagnostics on xenon for application to ion thrusters," *Proceedings of the 29th International Electric Propulsion Conference*, IEPC paper 2005–079, Princeton, NJ, 2005.

[34] Mazouffre, S., Bourgeois, G., Garrigues, L., and Pawelec, E., "A comprehensive study on the atom flow in the cross-field discharge of a Hall thruster," *J. Phys. D: Appl. Phys.*, Vol. 44, 2011, pp. 105203.

[35] Gawron, D., Mazouffre, S., Albarède, L., and Sadeghi, N., "Examination of Hall effect thruster acceleration layer characteristics by laser spectroscopy and repulsing potential analyzer," *Proceedings of the 42nd Joint Propulsion Conference*, AIAA paper 2006–4473, Sacramento, CA, 2006.

[36] Ngom, B. B., Smith, T. B., Huang, W., and Gallimore, A. D., "Numerical simulation of the Zeeman effect in neutral xenon from NIR diode-laser spectroscopy," *J. Appl. Phys.*, Vol. 104, 2008, pp. 023303.

[37] Barbieri, B., Beverini, N., and Sasso, A., "Optogalvanic spectroscopy," *Rev. Mod. Phys.*, Vol. 62, 1990, pp. 105203.

[38] Koslover, R. and McWilliams, R., "Measurement of multidimensional ion velocity distributions by optical tomography," *Rev.Sci. Instrum.*, Vol. 57, 1986, pp. 2441–2448.

[39] McWilliams, R. and Koslover, R., "Laboratory observation of ion conics by velocity-space tomography of a plasma," *Phys. Rev. Lett.*, Vol. 58, 1987, pp. 37–40.

[40] Zintl, M. and McWilliams, R., "Improved optical tomography device," *Rev. Sci. Instrum.*, Vol. 65, 1994, pp. 2574–2579.

[41] Packan, D., Jarrige, J., Elias, P.-Q., Cannat, F., Cucchetti, E., Vialis, T., and Lafleur, T., *Advanced diagnostics and thrusters: 3D laser induced fluorescence and electron cyclotron resonance thruster*, STO-AVT-VKI Lecture series 263; Electric propulsion systems, Von Karman Institute for Fluid Dynamics, T. Magin, Sint-Genesius-Rode, Belgium, 2016, pp. 12-1–12-61.

[42] Huang, W., Gallimore, A. D., and Smith, T. B., "Two-axis laser-induced fluorescence of singly-charged xenon inside a 6-kW Hall thruster," *Proceedings of the 49th Aerospace Sciences Meeting*, AIAA paper 2011–1015, Orlando, FL, 2011.

[43] Elias, P.-Q., Packan, D., Bonnet, J., Ceccanti, F., Cesari, U., Tata, M. D., and Gengembre, E., "Optical measurements of neutral cesium mass flow rate in field emission thrusters," *J. Propul. Power*, Vol. 27, 2011, pp. 448–460.

[44] Engeln, R., Mazouffre, S., Vankan, P., Schram, D. C., and Sadeghi, N., "Flow dynamics and invasion by background gas of a supersonically expanding thermal plasma," *Plasma Sources Sci. Technol.*, Vol. 12, 2001, pp. 595–605.

[45] Lejeune, A., Bourgeois, G., and Mazouffre, S., "Kr II and Xe II axial velocity distribution functions in a cross-field ion source," *Phys. Plasmas*, Vol. 19, 2012, pp. 073501.

[46] Vankan, P., Mazouffre, S., and Schram, R. E. D. C., "Inflow and shock formation in supersonic, rarefied plasma expansions," *Phys. Plasmas*, Vol. 12, 2005, pp. 102303.

[47] Mazouffre, S. and Bourgeois, G., "Spatio-temporal characteristics of ion velocity in a Hall thruster discharge," *Plasma Sources Sci. Technol.*, Vol. 19, 2010, pp. 065018.

[48] Mazouffre, S., Vankan, P., Engeln, R., and Schram, D., "Influence of surface chemistry on the transport of H atoms in a supersonic hydrogen plasma jet," *Phys. Plasmas*, Vol. 89, 2001, pp. 3824–3832.

[49] Vaudolon, J. and Mazouffre, S., "Indirect determination of the electric field in plasma discharges using laser-induced fluorescence spectroscopy," *Phys. Plasmas*, Vol. 21, 2014, pp. 096505.

[50] Pérez-Luna, J., Hagelaar, G. J. M., Garrigues, L., and Boeuf, J. P., "Method to obtain the electric field and the ionization frequency from laser induced fluorescence measurements," *Plasma Sources Sci. Technol.*, Vol. 18, 2009, pp. 034008.

[51] Spektor, R., "Computation of two-dimensional electric field from the ion laser induced fluorescence measurements," *Phys. Plasmas*, Vol. 17, 2010, pp. 093503.

[52] Kampschulte, T., Schulze, J., Luggenhölscher, D., Bowden, M. D., and Czarnetzki, U., "Laser spectroscopic electric field measurement in krypton," *New J. Phys.*, Vol. 9, 2007, pp. 18.

[53] Czarnetzki, U. and Sasaki, K., "Ultra-sensitive measurement of sheath electric fields by laser-induced fluorescence-dip spectroscopy," *J. Plasma Fusion Res.*, Vol. 83, 2007, pp. 215–227.

[54] Jiang, T., Bowden, M. D., Wagenaars, E., Stoffels, E., and Kroesen, G. M. W., "Diagnostics of electric fields in plasma using Stark spectroscopy of krypton and xenon atoms," *New J. Phys.*, Vol. 8, 2006, pp. 202.

[55] Booth, J. P., Fadlallah, M., Derouard, J., and Sadeghi, N., "Electric field measurements in discharges by 2+1 photon laser Stark spectroscopy of atomic hydrogen," *Appl. Phys. Lett.*, Vol. 65, 1994, pp. 819–821.

[56] Booth, J. P., Derouard, J., Fadlallah, M., Cabaret, L., and Pinard, J., "Electric field measurements in discharges by Doppler-free two-photon laser Stark spectroscopy of atomic hydrogen," *Optics Com.*, Vol. 132, 1996, pp. 363–370.

[57] Gavrilenko, V. P., Kim, H. J., Ikutake, T., Kim, J. B., Choi, Y. W., Bowden, M. D., and Muraoka, K., "Measurement method for electric fields based on Stark spectroscopy of argon atoms," *Phys. Rev. E*, Vol. 62, 2000, pp. 7201–.

[58] Jacobs, B., Gekelman, W., Pribyl, P., and Barnes, M., "Temporally resolved ion velocity distribution measurements in a radio-frequency plasma sheath," *Phys. Plasmas*, Vol. 18, 2011, pp. 053503.

[59] van der Heijden, H. W. P., Boogaarts, M. G. H., Mazouffre, S., van der Mullen, J. A. M., and Schram, D. C., "Time-resolved experimental and computational study of two-photon laser-induced fluorescence in a hydrogen plasma," *Phys. Rev. E*, Vol. 61, 2000, pp. 4402–4409.

[60] Vaudolon, J., Balika, L., and Mazouffre, S., "Photon counting technique applied to time-resolved laser-induced fluorescence measurements on a stabilized discharge," *Rev. Sci. Instrum.*, Vol. 84, 2013, pp. 073512.

[61] Vaudolon, J., Khiar, B., and Mazouffre, S., "Time evolution of the electric field in a Hall thruster," *Plasma Sources Sci. Technol. Fast Track Com.*, Vol. 23, 2014, pp. 022002.

[62] Vaudolon, J. and Mazouffre, S., "Observation of high-frequency ion instabilities in a cross-field plasma," *Plasma Sources Sci. Technol. Fast Track Com.*, Vol. 24, 2015, pp. 032003.

[63] Diallo, A., Keller, S., Shi, Y., Raitses, Y., and Mazouffre, S., "Time-resolved ion velocity distribution in a cylindrical Hall thruster: Heterodyne-based experiment and modeling," *Rev. Sci. Instrum.*, Vol. 86, 2015, pp. 022506.

[64] Durot, C. J., Gallimore, A. D., and Smith, T. B., "Validation and evaluation of a novel time-resolved laser-induced uorescence technique," *Rev. Sci. Instrum.*, Vol. 85, 2014, pp. 013508.

[65] MacDonald, N. A., Cappelli, M. A., and Hargus, W. A., "Time-synchronized continuous wave laser-induced fluorescence on an oscillatory xenon discharge," *Rev. Sci. Instrum.*, Vol. 83, 2012, pp. 113506.

[66] Fabris, A. L., Young, C. V., and Cappelli, M. A., "Time-resolved laser-induced fluorescence measurement of ion and neutral dynamics in a Hall thruster during ionization oscillations," *J. Appl. Phys.*, Vol. 118, 2015, pp. 233301.

[67] Mazouffre, S. and Bourgeois, G., "Spatio-temporal characteristics of ion velocity in a Hall thruster discharge," *Plasma Sources Sci. Technol.*, Vol. 19, 2010, pp. 065018.